

# Ultrafast entangling gates between nuclear spins using photo-excited triplet states

Vasileia Filidou\*,<sup>1</sup> Stephanie Simmons\*,<sup>1</sup> Steven D. Karlen,<sup>2</sup>  
Feliciano Giustino,<sup>1</sup> Harry L. Anderson,<sup>3</sup> and John J. L. Morton<sup>1,4</sup>

<sup>1</sup>*Department of Materials, University of Oxford,  
Parks Road, Oxford OX1 3PH, UK*

<sup>2</sup>*Northwestern University, Evanston, Illinois 60208-3113, USA*

<sup>3</sup>*Department of Chemistry, University of Oxford, Oxford OX1 3TA, UK*

<sup>4</sup>*CAESR, The Clarendon Laboratory, Department of Physics,  
University of Oxford, OX1 3PU, UK*

## CONTENTS

Characterisation of the DMHFP triplet	2
DFT calculations	2
Relaxation Kinetics	4
Triplet hyperpolarisation	5
Density matrix tomography	6
Nuclear spin state assignments	6
Measured density matrices	9
Coherence lifetimes	9
Density matrix fidelities	11
References	12

## CHARACTERISATION OF THE DMHFP TRIPLET

We performed pulsed and time-resolved ESR studies of the triplet state of DMHFP in order to fully characterise the spin Hamiltonian, relaxation rates and triplet polarisation.

The  $g$ -tensor was measured at X-band to be  $g_{xx} = 2.00076$ ,  $g_{yy} = 2.00224$ ,  $g_{zz} = 2.00274$  (with a  $g$ -strain approximately 0.1-0.2%). The zero-field splitting is characterised by:  $D_{xx} = 56.25$ ,  $D_{yy} = 164.33$ ,  $D_{zz} = -220.58$  MHz. The electron spin triplet  $T_1$  is longer than any of the observed triplet recombinations times, the longest of which is 267  $\mu$ s. In contrast,  $T_2$  is much shorter and was measured using a Hahn echo sequence to be  $\sim 3$   $\mu$ s.

### DFT calculations

In order to obtain an atomic scale understanding of our system we perform all-electron density-functional theory (DFT) calculations of the  $g$ -tensor and of the hyperfine tensor, for both the  $^1\text{H}$  and  $^{31}\text{P}$  nuclear spins in the excited spin-triplet electronic state. The calculations are performed using the ORCA<sup>2</sup> code within the generalized gradient approximation to DFT of Perdew, Burke, and Ernzerhof<sup>3</sup>, by expanding the electronic wavefunctions using the def2-SVP basis set (for preliminary geometry optimization), the def2-TZVP basis set<sup>4</sup>

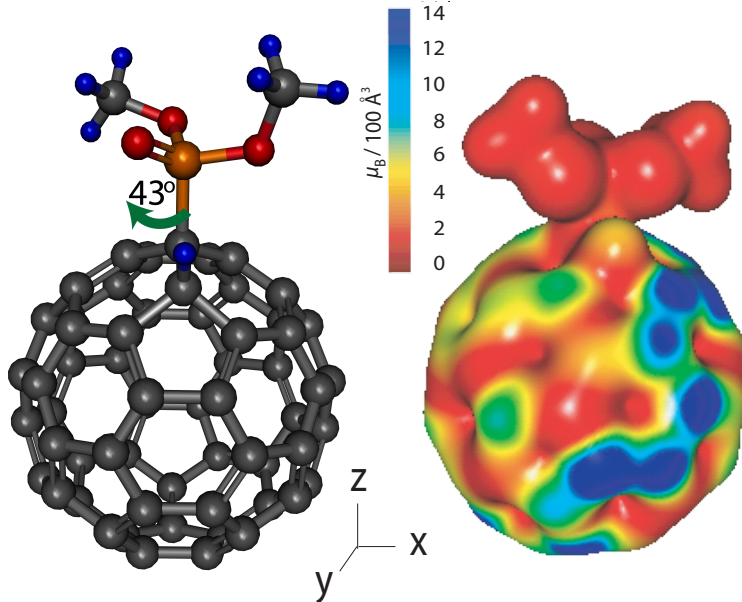


FIG. 1. **Optimised geometry of the DMHFP molecule in the tripled electronic state, and spin-density distribution.** (a) Ball-and-stick representation of the DMHFP molecule. In the optimized geometry the P=O bond forms a dihedral angle of  $43^\circ$  with the proton attached on the fullerene cage. Atomic color code: H (blue), C (grey), O (red), P (orange). (b) Colormap of the spin-density distribution in the triplet state, mapped on a electron density isosurface. The blue regions indicate high spin density. The image was rendered using `Gabedit`<sup>1</sup>.

(for accurate calculations of ground-state total energies), and the IGLOIII basis set<sup>5,6</sup> (for calculations of the  $g$ -tensor and of the hyperfine tensor). The ground-state geometry in the triplet state is determined by performing geometry optimizations starting from several initial configurations where the phosphonate adduct is rotated around the axis of the P=O bond. Each initial configuration corresponds to values of the dihedral angle between the P=O bond and the proton on the fullerene cage varying from  $0^\circ$  to  $180^\circ$  in steps of  $30^\circ$ ,  $0^\circ$  corresponding to the configuration where the P=O bond is eclipsed with the C-H bond of the cage. The conformation with the lowest energy has a dihedral angle of  $43^\circ$  and is 0.5 eV more stable than the conformation with the P=O at  $180^\circ$ . The length of the P-C bond in the ground-state geometry is 1.87Å. The calculated principal values of the  $g$ -tensor are 1.9999, 2.0018, and 2.0027, respectively, in good agreement with the corresponding experimental estimates 2.00076, 2.00224, and 2.00274.

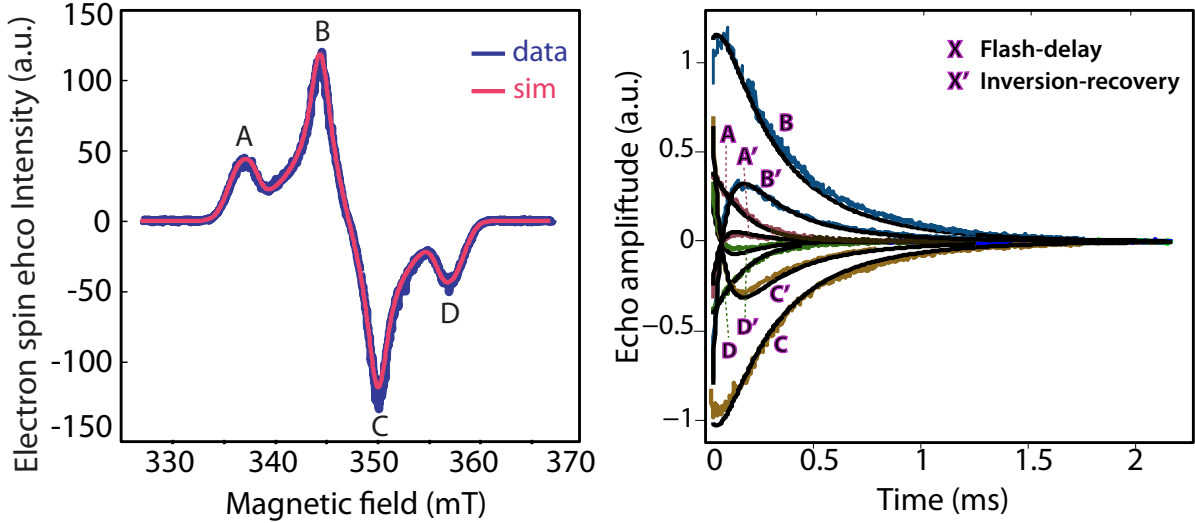


FIG. 2. **Flash-delay (FD) and inversion-recovery (IR) experiments at four magnetic field positions of the ESR spectrum marked A,B,C and D.** The fittings are in a very good agreement with the experiment and provide the initial populations of the triplet levels and the decay rates to the singlet. The  $T_y$  triplet level is the most populated and the one that decays slowest. In the simulations, no  $T_1$  relaxation between the sub-levels was required, indicating that the decay of the triplet state occurs at a rate fast compared to the relaxation  $T_1$ .

The calculated spin-density distribution in the triplet state is shown in Fig. 1. We observe that the spin density is localised around the fullerene cage, while negligible spin density appears on the phosphonate adduct. This is consistent with our previous calculations on a related fullerene derivative.<sup>7,8</sup>

The calculated isotropic components of the hyperfine tensors are  $A_{\text{iso}}(\text{H})=7.6$  MHz and  $A_{\text{iso}}(\text{P})=13.5$  MHz. These values are in good agreement with the measured Fermi contact terms  $A_{\text{iso}}(\text{H})=6$  MHz and  $A_{\text{iso}}(\text{P})=11$  MHz. The calculated principal values of the hyperfine tensors for the  $^1\text{H}$  nucleus are 7.0 MHz, 7.3 MHz, and 8.4 MHz, and the corresponding values for the  $^{31}\text{P}$  nucleus are 12.3 MHz, 12.4 MHz, and 16 MHz.

### Relaxation Kinetics

Flash-delay and inversion-recovery experiments were performed for the extraction of the decay rates, the lifetime of the triplet state and the populations of the triplet sublevels in

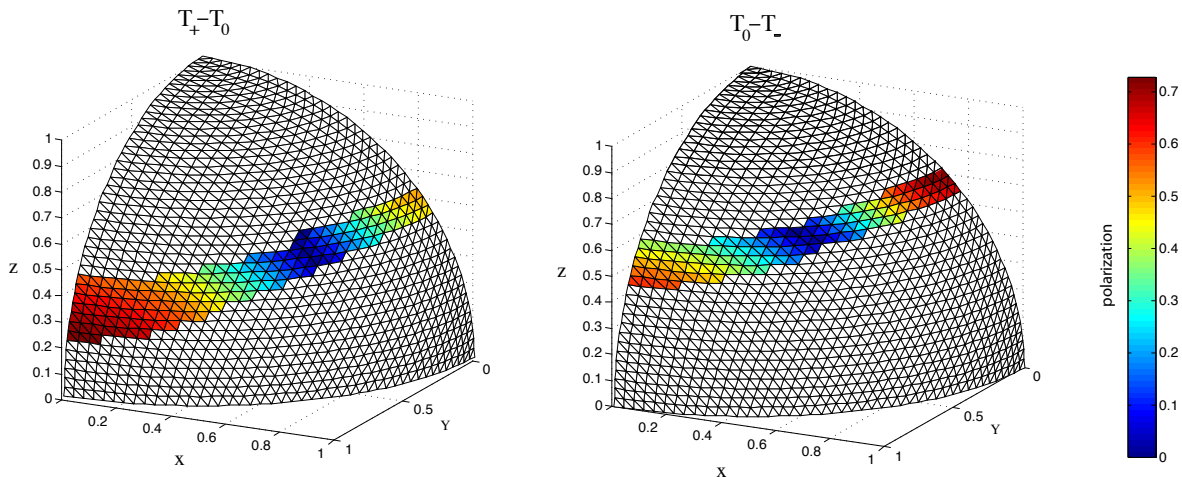


FIG. 3. Polarization of the  $T_+ : T_0$  and  $T_0 : T_-$  transitions at the molecular orientations on-resonance with 9.74 GHz at 349 mT. Polarization is observed up to 70% at certain orientations:  $\theta = 78 - 72^\circ$  and  $\phi = 0 - 10^\circ$  for  $T_+ : T_0$  and  $\theta = 48 - 52^\circ$  and  $\phi = 88 - 90^\circ$  for  $T_0 : T_-$ .

X-band (Figure 2). For the simulations of each decay we averaged a weighted distribution of the spins for all the orientations at each magnetic field including a variation of the tip angle of the inversion pulse. For all simulated decay curves, the same set of parameters was used: the populations of the zero-field eigenstates  $T_{x,y,z}$  were:  $p_x = 0.22$ ,  $p_y = 0.71$ ,  $p_z = 0.01$ , and the decay rates from these levels were  $k_x = 11000 \text{ s}^{-1}$ ,  $k_y = 1900 \text{ s}^{-1}$  and  $k_z = 28000 \text{ s}^{-1}$ . The populations give a polarisation ratio of 0.33 which is in good agreement with the polarisation ratio obtained from the electron spin echo-detected field sweep spectrum.

### Triplet hyperpolarisation

At a given magnetic field, a number of molecular orientations with respect to the applied magnetic field may be on resonance with the applied microwave pulses. Figure 3 illustrates those orientations on resonance at 349 mT (the field used in our study), and shows the triplet state polarization of the relevant electron spin transition (i.e.  $T_+ : T_0$  or  $T_0 : T_-$ ). We observe that the differences in population between the in field triplet sub-levels depend heavily on the orientation, while the average polarization is about 35–40%

# DENSITY MATRIX TOMOGRAPHY

## Nuclear spin state assignments

Quantum state tomography can be performed using a variety of techniques, and the basic method employed in this work is described in detail elsewhere<sup>9</sup>. The process involves mapping the populations and coherences of the quantum state under investigation onto fixed observables – in this case,  $\mathbf{E}(S_y)$ ,  $\mathbf{E}(S_x)$ , the  $\sigma_Y$  and  $\sigma_X$  expectation values for all electron spin transitions resonant with a particular frequency at a fixed magnetic field.

Contributions to these observables come from a variety of molecular orientations, and for each orientation the microwave transition is on-resonance with a particular nuclear eigenstate in  $T_0$  and its matching nuclear spin state in  $T_+$  or  $T_-$ . We define  $|4\rangle$  as this orientation-dependent nuclear spin state, which is well-defined due to the system's large  $D$  and  $A$  values. The effective eigenstates  $|3\rangle$  and  $|2\rangle$  differ from  $|4\rangle$  by a  $^1\text{H}$  and  $^{31}\text{P}$  spin flip, respectively, and  $|1\rangle$  differs from  $|4\rangle$  by a flip of both nuclear spins.

Population differences and coherence amplitudes within the  $T_0$  subspace are first mapped to the eigenstate  $|4\rangle$  in  $T_0$  for readout, where readout is done by measuring the population difference (measured via spin-echo amplitudes) between the nuclear state  $|4\rangle$  in  $T_0$  and the matching nuclear state  $|4\rangle$  in  $T_+$  or  $T_-$  as appropriate.

The amplitudes and phases of the single quantum coherences are measured by labeling the coherences with time-varying phases applied with  $\sigma_Z$  gates and then projecting these coherences onto the state  $|4\rangle$  with a fixed-phase  $\pi/2$  pulse. This results in an oscillation in the final observable with a frequency given by the applied phase increment per experimental shot<sup>10</sup>. A normalised Fourier transform of this oscillation reveals the amplitude and phase of the single quantum coherences in the effective density matrix expressed in the basis  $\{|1\rangle, |2\rangle, |3\rangle, |4\rangle\}$ .

The  $\sigma_Z$  operations can be applied geometrically with two  $\pi$  pulses about different rotation axes: a  $\sigma_Z$  rotation of angle  $\varphi$  applied to  $^{31}\text{P}$  followed by a  $\sigma_Z$  rotation of angle  $\theta$  applied to

$^1\text{H}$  results in the unitary:

$$U = \begin{pmatrix} e^{+i\varphi/2+i\theta/2} & 0 & 0 & 0 \\ 0 & e^{+i\varphi/2-i\theta/2} & 0 & 0 \\ 0 & 0 & e^{-i\varphi/2+i\theta/2} & 0 \\ 0 & 0 & 0 & e^{-i\varphi/2-i\theta/2} \end{pmatrix} \quad (1)$$

The application of  $U^i$ , for  $i$  the increment number, results in various frequencies (rotation/increment), some of which are shared: this process does not distinguish between the coherences  $|1\rangle\langle 3|$  and  $|2\rangle\langle 4|$ , nor between the coherences  $|1\rangle\langle 2|$  and  $|3\rangle\langle 4|$ . This is acceptable given high-fidelity nuclear  $\pi$  pulses and the fact that the final measurement only measures the population difference between  $|4\rangle$  and its matching nuclear eigenstate in  $T_-$  or  $T_+$ .

Depending upon the nuclear spin composition of  $|4\rangle$ , the coherence  $|1\rangle\langle 4|$  will either be a zero- or a double-quantum coherence. Under the application of  $U^i$  the resulting frequency will either be the sum of the absolute value of the two frequencies (in the case of a DQC) or the difference (in the case of a ZQC). Both frequencies are indeed observed in measurements of the coherences  $|4\rangle\langle 1|$  and  $|3\rangle\langle 2|$  (See Figure 4). Simulations of these sequences applied to each of the four nuclear input states confirm this response.

These simulations were used to ascertain if pulse errors could erroneously assign ZQCs a DQC frequency and vice versa, or if pulse errors contributed to greater decoherence of one coherence over that of another. The sequence was simulated with typical nuclear spin dephasing rates (due to  $B_0$  inhomogeneities) and rotation errors (due to  $B_2$ , or RF pulse power inhomogeneities). Pulse errors were sampled from a standard deviation in the rotation angle of each pulse, and these errors were taken to be maximally correlated. No ‘mislabeling’ errors were observed for a range of pulse errors from negligible errors up to the point where the standard pulse rotation error was a  $\pi$  rotation and the dephasing rate was an order of magnitude faster than experimentally recorded.

The ratio of the ZQC to DQC in the coherences  $|1\rangle\langle 4|$  and  $|2\rangle\langle 3|$  were measured to be roughly 1:3 and 3:1, respectively. The pulse sequence simulations indicate that this unequal distribution of populations is not due to pulse or dephasing errors but rather due to the composition of the state  $|4\rangle$  itself. We infer from the resulting data that the composition of  $|4\rangle$  is mostly made up of the  $|\downarrow, \downarrow\rangle$  and  $|\uparrow, \uparrow\rangle$  nuclear states. For this reason, the sum of the shared-phase ZQC and DQC frequency components are used to infer the amplitude and phase of the entangled quantum coherences.

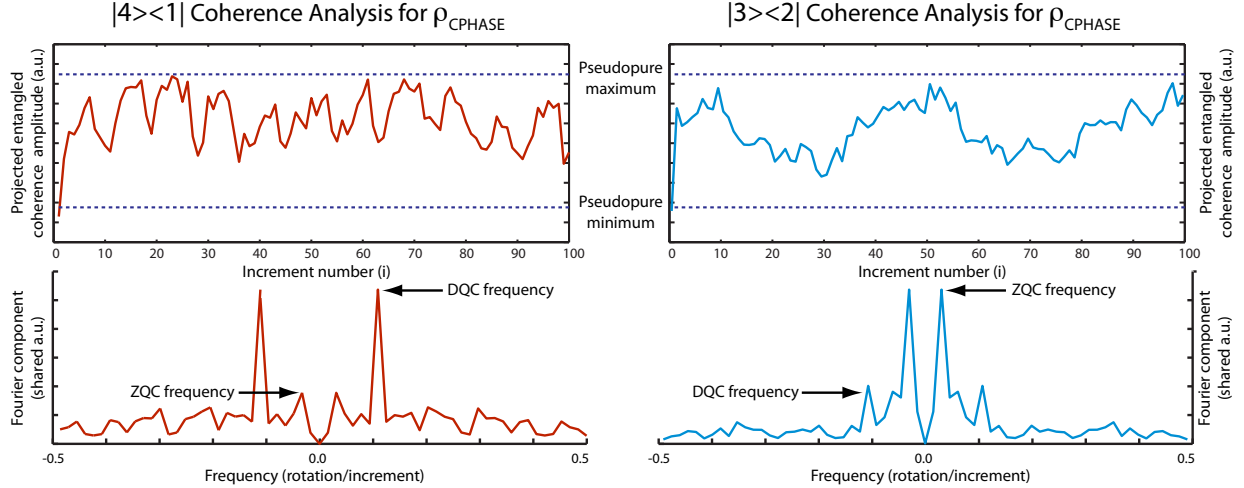


FIG. 4. **Coherence analysis.** The CPHASE entangling operations can be used to generate either a ZQC or a DQC and the observed oscillations due to the tomography process are shown above. Fourier analysis of both measurements reveal contributions from the other multiple quantum coherence, which could be due to systematic pulse errors or due to the composition of  $|4\rangle$ .

The spin Hamiltonian does not reveal any large initial nuclear polarisation at the chosen field and frequency. The source of this nuclear polarisation may arise from the linearly-polarised incident laser light, a nuclear spin-dependent ISC or other spin-dependent relaxation mechanism, and is a subject of future study.

In DMHFP there are six hydrogen spins on methyl groups (with weak triplet hyperfine couplings) that in principle exhibit dipolar couplings to the single  $^{31}\text{P}$  spin in addition to the single  $^1\text{H}$  spin bonded to the cage. We rule out their contribution to the 3 kHz measured by the SEDOR sequence, by running the same sequence on both the  $^{31}\text{P}$  spin, and the  $^1\text{H}$  spin directly bonded to the cage, and in each case measure the same coupling.

## Measured density matrices

The final density matrix for the SEDOR-based method is:

$$\begin{pmatrix} 0.247 & -0.006 - 0.001i & -0.015 - 0.007i & 0.123 \\ -0.006 + 0.001i & 0.338 & -0.009 + 0.010i & -0.014 + 0.002i \\ -0.015 + 0.007i & -0.009 - 0.010i & 0.160 & -0.012 + 0.001i \\ 0.123 & -0.014 - 0.002i & -0.012 - 0.001i & 0.255 \end{pmatrix} \quad (2)$$

The final density matrix for the CPHASE-based method is:

$$\begin{pmatrix} 0.391 & -0.068 - 0.105i & 0.012 - 0.011i & 0.271 \\ -0.068 + 0.105i & 0.116 & 0.017 + 0.007i & 0.005 - 0.011i \\ 0.012 + 0.011i & 0.017 - 0.007i & 0.130 & 0.095 - 0.085i \\ 0.271 & 0.005 + 0.011i & 0.095 + 0.085i & 0.364 \end{pmatrix} \quad (3)$$

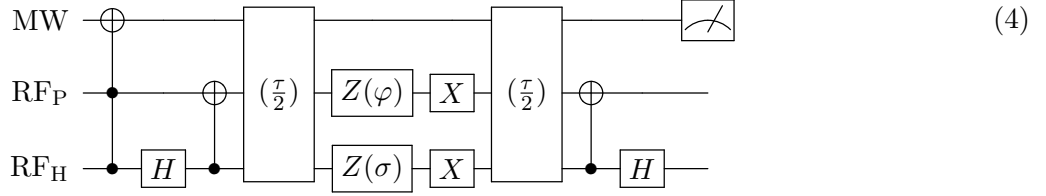
Uncertainties due to signal noise account for less than 0.005 and 0.002 each density matrix element for the SEDOR- and CPHASE-based matrices, respectively. These measurements do not include corrections for known pulse rotation errors in the tomography sequence or signal degradation due to spin relaxation, which would both augment the reported fidelity.

## Coherence lifetimes

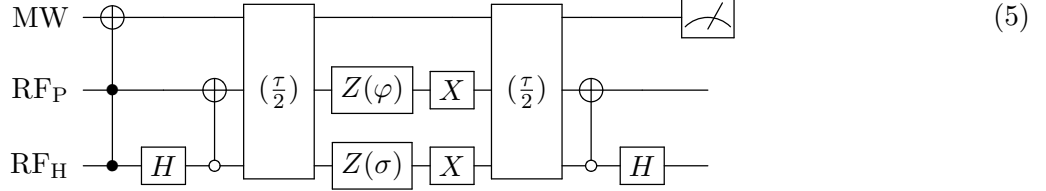
The  $T_{1P}$  and  $T_{1H}$  times limit the lifetime of the ZQC/DQC coherences and can be measured with a nuclear spin inversion-recovery experiment with a fixed final spin echo time. The times measured using this sequence exceed the lifetime of the triplet electron spin and so are not expected to play a role in the reduced ZQC/DQC amplitude. The  $T_{2P}$  and  $T_{2H}$  times, measured to be 1.9(4) ms and 0.20(4) ms respectively using a two-step phase-cycled nuclear spin echo sequence, can provide a rough estimate for the decay rate of the entangled quantum coherence.

The lifetimes of an entangled coherence can be measured directly by extending the length of time on either side of the phase gates in the sequence given in Figure 5. These sequences involve refocussing pulses applied to both spins at the midway point: flipping both spins reverses the phase of a DQC or ZQC, but does not change one into the other. The lifetimes of both a ZQC and a DQC coherence can be measured in this way and the results are shown in Figure 6.

**DQC lifetime measurement:**



**ZQC lifetime measurement:**



**Refocused ZQC/DQC measurement:**

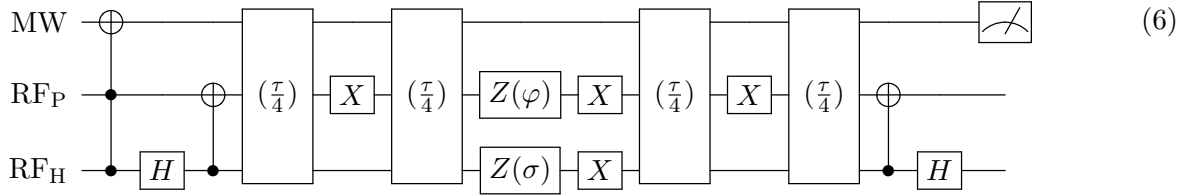


FIG. 5. **Measuring lifetimes with DMHFP.** These sequences are used to determine the lifetimes of the ZQC and DQC coherences, as well as to test the effects of the dipolar coupling upon these coherences by refocusing its effects. The delay wait( $\tau$ ) is written as just the time  $\tau$ , the Hadamard matrix is implemented using a  $\pi/2$  pulse, and the meter at the end of each sequence represents a microwave spin-echo population measurement.

A decoupling scheme involving a  $\pi$  pulse on each nuclear spin midway through the sequence does not refocus the dipolar coupling. This is indeed the way that nuclear couplings are used to perform a CNOT operation, and these effects contribute to a modulation of the ZQC and DQC amplitudes with a frequency of 3 kHz. The decay of these coherences is monotonic with  $T_{2,\text{DQC}} \approx 100 \mu\text{s}$  and  $T_{2,\text{ZQC}} \approx 200 \mu\text{s}$ , indicating an additional source of decoherence which affects the multiple quantum coherences. To confirm that the dipolar coupling is not playing a role in the measured ZQC and DQC decoherence times, a decoupling sequence can be used which removes the effects of the dipolar coupling. Additional refocusing pulses are applied to a single nucleus at the one-quarter and three-quarter points during this delay. This sequence, shown in Figure 5, takes an entangled quantum coherence

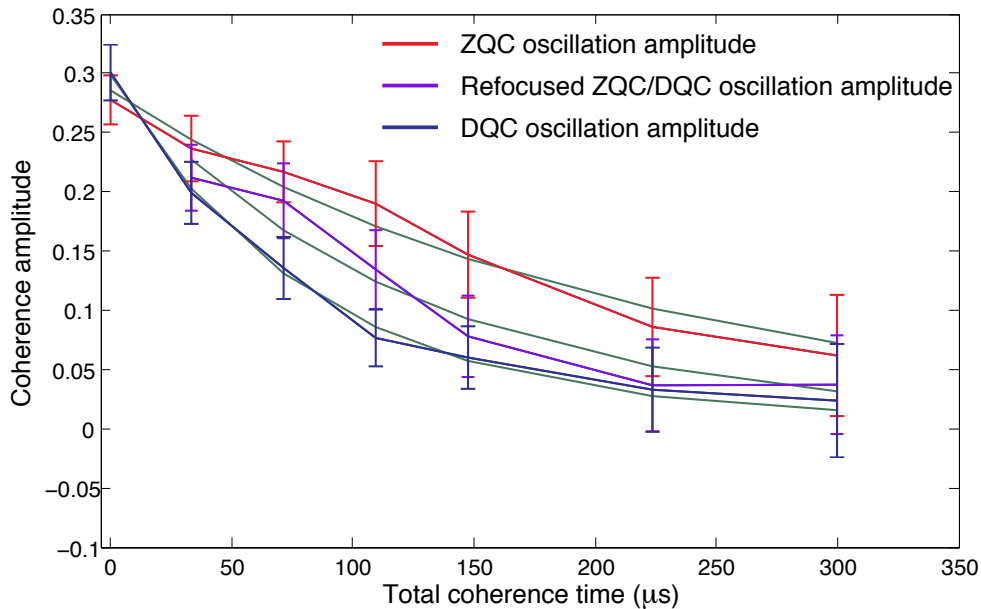


FIG. 6. **Entangled coherence lifetimes.** Results of the measurements of various lifetimes of the system are shown above. Both the ZQC and the DQC coherences are limited by the  $^1\text{H}$  nuclear  $T_2$  time. By decoupling the effects of the dipolar coupling one sees no improvement to this lifetime, indicating that this shortened lifetime is due to some other source of dephasing in the system. Here  $T_{2,\text{DQC}} \approx 100 \mu\text{s}$  and  $T_{2,\text{ZQC}} \approx 200 \mu\text{s}$ .

through each of the four pseudopure Bell states, and so although it refocuses the effects of dipolar coupling, it should yield an average of the DQC and ZQC decoherence rates. Indeed, the results shown in Figure 6 reveal a lifetime midway between the ZQC and DQC, confirming that the dipolar coupling plays no dominant role in the faster relaxation mechanism of the multiple quantum coherences.

### Density matrix fidelities

There are two conventional measures of state fidelity,  $\mathcal{F}(\rho_1, \rho_2) = (\text{Tr}(\sqrt{\sqrt{\rho_2}\rho_1\sqrt{\rho_2}}))^2$  or alternatively the more generous measure  $\sqrt{\mathcal{F}(\rho_1, \rho_2)}$ . When applied to physically allowed states, both measures are non-negative and reach a maximum value of 1 when  $\rho_1 = \rho_2$ . For this work the more conservative measure is used.

Taking into account these relaxation times, the maximum expected fidelities for the pseudo-entangled states with uniform dipolar coupling and geometric entangling operations

amount to 68% and 85%, respectively. These fast relaxation times largely account for the low recovered fidelities of the of the pseudo-entangled states (34% and 65% respectively<sup>11</sup>), indicating that the overall limitations with this entangling approach are the natural lifetimes of the system. As stated in the main text, the residual imperfection is due to the limited fidelity of the CPHASE operation and small gate imperfections, consistent with simulations incorporating a 4% error on each nuclear gate in the sequence.

- 
- [1] Allouche, A. R. Gabedit, a graphical user interface for computational chemistry softwares. *Journal of Computational Chemistry* 174 (2011).
- [2] Neese, F. *ORCA, An ab Initio, Density Functional and Semiempirical Program Package version 2.8* (University of Bonn, Germany, 2010).
- [3] Perdew, J. P., Burke, K. & Ernzerhof, M. Generalized gradient approximation made simple. *Phys. Rev. Lett.* **3865** (1996).
- [4] Schaefer, A., Horn, H. & Ahlrichs, R. Fully optimized contracted gaussian basis sets for atoms Li to Kr. *J. Chem. Phys* **97** (1992).
- [5] Schindler, M. & Kutzelnigg, W. J. Theory of magnetic susceptibilities and NMR chemical shifts in terms of localized quantities. II. Application to some simple molecules. *J. Chem. Phys.* **76** (1982).
- [6] Kutzelnigg, W., Fleischer, U. & Schindler, M. *The IGLO Method: Ab Initio Calculation interpretation of NMR chemical shifts Magnetic Susceptibilities* (Springer-Verlag:Heidelberg, Germany, 1990).
- [7] Schaffry, M. *et al.* Entangling remote nuclear spins linked by a chromophore. *Phys. Rev. Lett.* **104** (2010).
- [8] Filidou, V., Ceresoli, D., Morton, J. J. L. & Giustino, F. First-principles investigation of hyperfine interactions for nuclear spin entanglement in photo-excited fullerenes. *Phys. Rev. B* (submitted).
- [9] Simmons, S. *et al.* Entanglement in a solid-state spin ensemble. *Nature* **470**, 69–72 (2011).
- [10] P. Höfer. Multiple quantum pulsed ENDOR spectroscopy by time proportional phase increment detection. *App. Magn. Res.* **11** (1996).
- [11] These times do not compare favourably to a randomly generated state which would on average

have a fidelity of 25%, however the pseudo-entangled state is generated in much less time than the total tomography sequence time, allowing one to infer a much higher fidelity at the time of generation.